the FEBS Journal

Understanding the binding properties of an unusual metal-binding protein – a study of bacterial frataxin

Chiara Pastore[1], Marisa Franzese[2], Filomena Sica[2,3], Pierandrea Temussi[1,2] and Annalisa Pastore[1]

1 National Institute for Medical Research, London, UK
2 Dipartimento di Chimica, University of Naples, Italy
3 Istituto di Biostrutture e Bioimmagini, CNR, Naples, Italy

Keywords
CyaY; Friedreich's ataxia; iron binding; NMR; X-ray

Correspondence
A. Pastore, NIMR, The Ridgeway, London, NW71AA, UK
Fax: +44 20 89064477
Tel: +44 20 88162630
E-mail: apastor@nimr.mrc.ac.uk

(Received 3 April 2007, revised 28 May 2007, accepted 18 June 2007)

doi:10.1111/j.1742-4658.2007.05946.x

Deficiency of the small mitochondrial protein frataxin causes Friedreich's ataxia, a severe neurodegenerative pathology. Frataxin, which has been highly conserved throughout evolution, is thought to be involved in, among other processes, Fe–S cluster formation. Independent evidence shows that it binds iron directly, although with very distinct features and low affinity. Here, we have carried out an extensive study of the binding properties of CyaY, the bacterial ortholog of frataxin, to different divalent and trivalent cations, using NMR and X-ray crystallography. We demonstrate that the protein has low cation specificity and contains multiple binding sites able to chelate divalent and trivalent metals with low affinity. Binding does not involve cavities or pockets, but exposed glutamates and aspartates, which are residues that are unusual for iron chelation when not assisted by histidines and/or cysteines. We have related how such an ability to bind cations on a relatively large area through an electrostatic mechanism could be a valuable asset for protein function.

Friedreich's ataxia is a severe neurodegenerative pathology that, by affecting the central nervous system and the myocardium, leads to progressive loss of voluntary muscle movement and, ultimately, to death. It is caused by deficiency of frataxin, a small mitochondrial protein [1], that is remarkably conserved throughout evolution, from purple bacteria to humans. The protein is essential for life, as supported by the observation that frataxin knockout mice die *in utero* shortly after implantation [2]. Different and sometimes conflicting functions have been proposed for frataxin. It has been suggested to act as an iron chaperone [3–6], to act as an iron storage protein with properties similar to those of ferritin [7–9], or to be involved in Fe–S cluster assembly, in oxidative stress, in heme biosynthesis, or in iron homeostasis [4,10–19]. Although it remains unclear which of these hypotheses reflects most closely the cellular role of frataxin, their common denominator is a link between frataxin and iron.

Interestingly, frataxin is itself an iron-binding protein, although with features distinctly different from those of any other protein with this property [20]. Knowledge of the frataxin fold from bacteria, yeasts and humans has shown that the protein does not contain cavities or pockets that could host iron or a suitable prosthetic group [21–25]. In addition, it does not contain conserved histidines and/or cysteines, the residues usually implicated in iron chelation. The iron-binding surface has been mapped onto a semiconserved negatively charged ridge that contains several semiconserved glutamate and aspartate side chains [21,24,25]. In agreement with the absence of features that are assumed to be essential for providing the correct geometry in iron chelation, the affinities of iron in frataxin–iron complexes have been shown to be weak, being at the very best in the micromolar range [3,26].

An unbiased approach towards a better understanding of the cellular function of frataxin is to characterize further the mode of iron coordination and to investigate the selectivity and specificity of this interaction. Previous work has shown that frataxins from *Homo sapiens*, yeast and *Escherichia coli* bind, although with comparably modest affinities, both Fe(II) and Fe(III) in corresponding protein regions,

suggesting that iron binding is relevant for its function [21,24,25]. Solid evidence has also associated these three orthologs with similar metabolic pathways. Here, we have extended the solution study of frataxin's binding properties to different cations that are either close to iron in the periodic table or share with it similar properties, with the aim of understanding binding specificity. We have used both NMR techniques, for studying binding in solution, and X-ray crystallography, for solving the structures of the complexes with cobalt and europium. Among all frataxins, we selected as a model system CyaY, the bacterial ortholog of human frataxin, as previous extensive studies on this protein have shown that, while sharing high homology with eukaryotic frataxins (27% similarity and 45% homology with the human protein), it has several features that make it a more reliable model system than either the yeast (Yfh1) or the human orthologs: CyaY is a 106 residue protein ($\sim$ 12.2 kDa) that comprises only the evolutionarily conserved domain common to all frataxin orthologs, without addition of mitochondrial import signals [24]. Although CyaY has similar iron-binding properties to Yfh1 [27], it is relatively more stable in terms of both thermal stability and fold [28], and gives excellent NMR spectra [24]. Finally, a bacterial model system could simplify the study of frataxin's role in Fe–S cluster formation, as in bacteria this machinery is confined in well-defined operons.

The view that emerges from our study is that frataxin has low specificity for iron and can accommodate in the same pocket almost any divalent/trivalent cation, using a geometry of interaction that seems unique to this protein.

Results

Solution studies

The main tool used in our solution studies was the perturbation of the [^{1}H,^{15}N]-HSQC NMR correlation spectrum caused by addition of increasing amounts of different cations. This method, introduced in the 1970s [29], remains a powerful tool with which to explore ion binding. We first revisited in a systematic way the effects of increasing quantities of iron (Fe^{2+} and Fe^{3+}) on the [^{1}H,^{15}N]-HSQC NMR spectrum of CyaY, and then compared these findings with the corresponding effects produced by other divalent and trivalent cations. Our results are summarized in Fig. 1A, which shows all perturbations of NMR parameters caused by different ions. It is possible to grasp at a glance that the region of the protein sequence affected is roughly the same for all the cations explored (Fig. 1B), irrespective of their charge density and/or specific electronic properties. In order to discriminate between different ions, we need to examine each titration in detail.

Titration of CyaY with Fe^{2+} and Fe^{3+}

Addition of Fe^{2+} induced the displacement of several resonances in the [^{1}H,^{15}N]-HSQC NMR spectrum of CyaY, but the most striking consequence of the addition was the total disappearance of specific resonances without the concomitant appearance of other signals in other parts of the spectrum. This result could be a consequence of the paramagnetic properties of Fe(II), or it might arise from the presence of an intermediate equilibrium rate between the free and the bound forms. In the latter case, the line broadening caused by the dynamic process could be extremely large and unspecific, preventing the detection of most peaks. On the contrary, we observed specific effects even at very low ion/protein ratios: at a 1 : 1 Fe^{2+}/protein ratio, the resonances of Arg20, Asp22 and Asp23 disappeared, and the resonance of Leu21 shifted. At a 2 : 1 ratio, the resonances of residues 19 and 44 also disappeared, whereas those of residues 24, 28, 29, 31, 32 and 33 shifted. At a stoichiometric ratio of nearly 6 : 1, several resonances were affected, as expected from the effect of bulk paramagnetism of the free paramagnetic $Fe(H_2O)^{2+}$ that affects indiscriminately all the exposed residues.

When spectral changes were monitored following titration with Fe(III), the most affected resonances at a 1 : 1 protein/iron ratio were again those of Arg20, Leu21, Asp22 and Asp23. At a 1 : 2 ratio, the above resonances disappeared completely, together with those of the amides of residues 29, 30 and 31. At a 1 : 6 protein/iron ratio, the resonances of residues 19–35 were completely bleached, whereas those of residues 42, 44, 104 and 105 were only slightly affected. At higher Fe^{3+}/protein ratios, we noticed an overall line broadening, albeit smaller than the one observed in the titration with Fe^{2+}. The difference can be attributed to the fact that the excess of Fe(III) is not found as free ions in solution but is bound to protein aggregates, which form at high iron/protein ratios [9,26]. Large molecular species would not be detectable by NMR, and are likely to sequester the free paramagnetic species from solution.

Titration of CyaY with Ca^{2+} and Mg^{2+}

We resorted to two divalent cations, Ca^{2+} and Mg^{2+}, to test the specificity of the iron-binding sites. Both cations, which have been shown to compete with

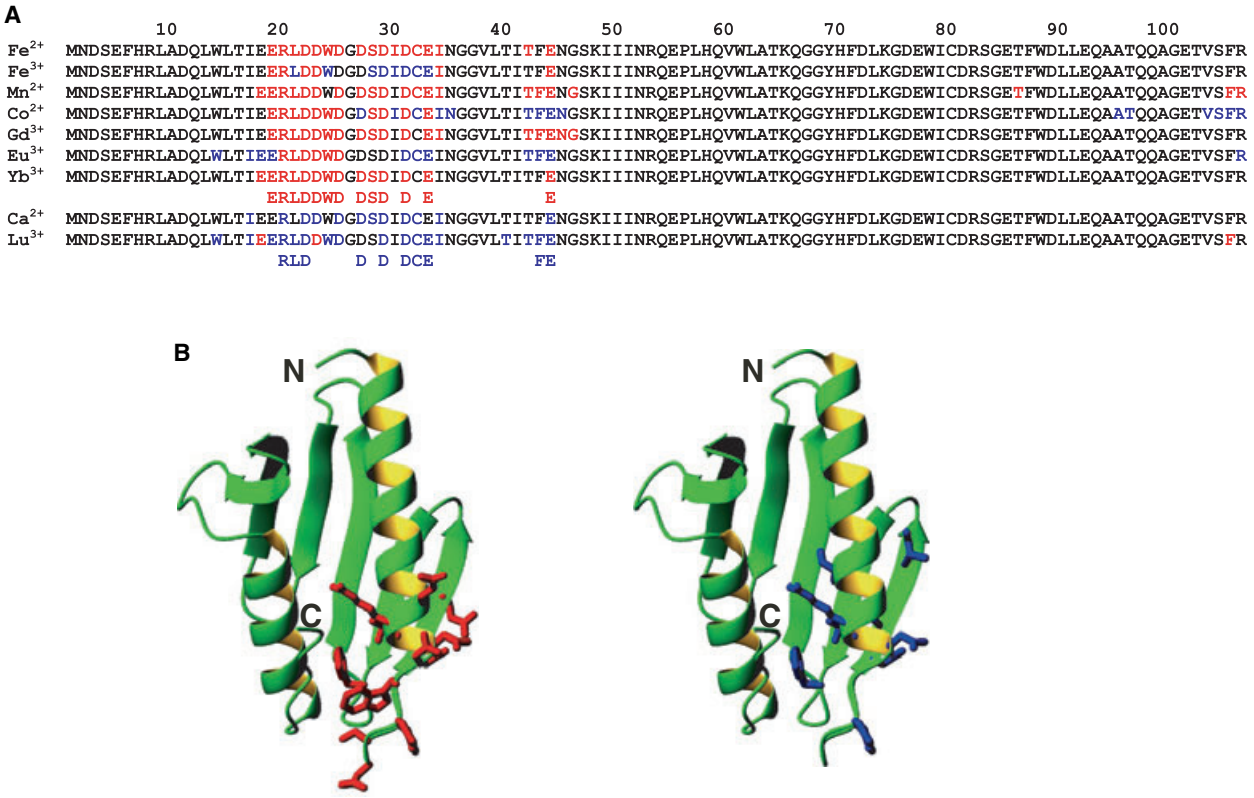

Fig. 1. Perturbations of the NMR spectra caused by different ions. (A) Summary of the residues affected by the addition of different ions. Residues are highlighted in red when mainly broadened or in blue when mainly shifted. A consensus, selected for most affected residues in at least 50% of the cases, is shown for paramagnetic and diamagnetic ions. Zn^{2+} is not reported, as this cation seems to have a more unspecific role and to promote aggregation rather than to bind specifically to the protein. (B) Ribbon representations of CyaY (1ew4) on which the consensus residues are mapped into the structure. The residues that broaden after titration with paramagnetic cations are indicated in red (left), whereas in the residues whose resonances are shifted by diamagnetic cations are in blue. The figure was generated by MOLMOL [45].

Fe(III)-promoted aggregation [26,27], are diamagnetic and can therefore help in the unambiguous identification of the binding site without the interference of paramagnetic effects. We recorded [^{1}H,^{15}N]-HSQC spectra at increasing Ca^{2+}/protein ratios. Also with this ion, the first resonances to be affected were the amides of residues 14, 17, 22, 23, 25, 27–32, 34 and 44, which were shifted without any appreciable line broadening, indicating a change of the chemical environment around the binding site upon binding of the diamagnetic Ca^{2+} (Fig. 2C). No other resonances were affected at higher ratios, and the chemical shift variation reached a plateau at an approximately 1 : 6 protein/Ca^{2+} ratio. The effect, which only implies chemical shift changes, was, however, very small (on average less than 0.02 p.p.m. in the proton dimension), suggesting a weak interaction (i.e. in the millimolar range).

To test the effect of Mg^{2+}, we carried out a titration up to a 5 : 1 Mg^{2+}/CyaY ratio, but did not notice any variation of the signals. We cannot, however, exclude the possibility that this cation could bind at higher ratio, thus explaining its observed ability to compete with iron-induced aggregation [27]. To verify the consistency of the experiment, we added to the solution five equivalents of Ca^{2+}. As previously noted, the presence of Ca^{2+} induced small shifts, among which is the diagnostic downfield shift of the amide of Asp23.

Titration of CyaY with Mn^{2+} and Co^{2+}

Co^{2+} and Mn^{2+} were tested because they have an ionic radius similar to that of Fe^{2+}. Being highly paramagnetic ions, they are expected to have strong effects at very low ion/protein ratios.

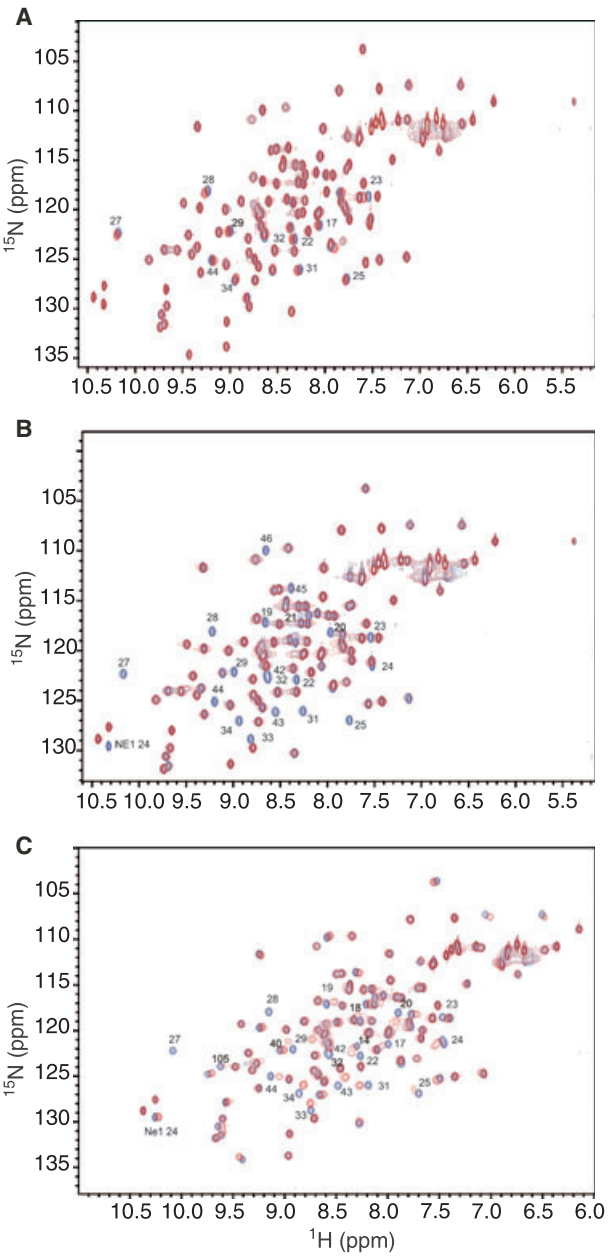

Fig. 2. Representative HSQC spectra of CyaY titrations. Superimpositions of a reference [^{1}H,^{15}N] HSQC spectrum of CyaY (blue) with a spectrum (red) of a 1 : 1 mixture of CyaY/Gd^{3+} (A), a 1 : 1 mixture of CyaY/Lu^{3+} (B), and a 1 : 2 mixture of CyaY/Ca^{2+} (C).

Co^{2+} can be high spin or low spin, according to its coordination sphere. High-spin and low-spin geometries induce narrow broadening (2–100 Hz, depending on the coordination number) and large broadening (200–1000 Hz), respectively [30]. We observed strong relaxation enhancement and shift variations at 0.5 equivalents: the resonances of residues 19–22, 24, 25, 28, 29, 31 and 33 disappeared, those of residues 23 and 45 were affected by severe line broadening, whereas those of residues 27, 30, 32, 34, 35, 40, 42–44, 95, 96, 103, 104 and 105 were shifted. The strong effect of this cation on the spectrum of CyaY prevented further analysis at higher cation/protein ratios.

Mn^{2+} is a d^5 ion with a strong paramagnetic NMR effect, having a long relaxation time and a line broadening of 100 000 Hz [30]. This ion has been previously used to mimic the behavior of Fe(II), because of the similarity of ionic radii and paramagnetic properties [31]. It should produce efficient line broadening of atoms closer than 5 Å. Accordingly, complete bleaching of the resonances of residues 19–34, 42–46 and 105–106 was observed at a 0.1 : 1 Mn^{2+}/CyaY ratio.

The strong paramagnetic properties of Mn^{2+}, which can sometimes mimic those of Fe^{2+} without the difficulties of keeping the sample under anaerobic conditions, were exploited to study the relative ability of Mn^{2+} to compete for binding with the probably more abundant Ca^{2+} and Mg^{2+}. We tested its effect in the presence of a Ca^{2+}/Mg^{2+}/CyaY mixture at a 5 : 5 : 1 ratio. Upon addition of 0.1 equivalents of Mn^{2+}, we observed bleaching of the same peaks that are affected in the titration of the apoprotein. We observed, in particular, the disappearance of residue 23. This suggests that Mn^{2+} can displace Ca^{2+} at very low concentrations, thus enabling it to compete effectively with this ion. If we assume that the behavior of Fe(II) is similar to that of Mn^{2+}, we should conclude that the presence of Ca^{2+} and Mg^{2+} in the cells cannot interfere with CyaY iron binding.

Titration of CyaY with Zn^{2+}

Zn^{2+} is involved in several essential biological functions. Titration of CyaY with this cation induced large perturbations at substoichiometric cation/protein ratios (0.5 : 1) (supplementary Fig. S1A). The resonance of residue 12 disappeared completely. Several other peaks in the HSQC spectrum showed a reduction in intensity without significant chemical shift variations. Among these were residues 5, 10–18, 20, 21, 39, 53–55, 57, 60, 61, 70–73 and 75, and the indole side chains of Trp61 and Trp78, both of which are either completely or partially exposed to the solvent. Interestingly, the resonance of residue 23, which was one of the first affected by most of the other cations, remained unperturbed. Further titration (1 : 1) bleached almost completely these resonances and, in addition, affected those of residues 34, 35, 37, 39 and 80 (supplementary Fig. S1B). At a 1.5 : 1 ratio, most resonances disappeared. As Zn^{2+} is diamagnetic, these results are

compatible with a Zn^{2+}-promoted salting-out phenomenon, rather than with specific binding. Aggregation seems to initiate around the first helix.

Titration of CyaY with lanthanides – the effect of europium and ytterbium

Lanthanides were used to enhance the paramagnetic effects around the binding site: they induce a line broadening of 1–100 Hz in nuclei located within 5 Å of the binding site, depending on the molecular mass of the protein and the strength of the magnetic field. The only exceptions are gadolinium (as Gd^{3+}), which has a much stronger effect, with signal broadening of 20 000–200 000 Hz [30], and lanthanium and lutetium, which are diamagnetic.

Titration with Eu^{3+} was first followed by TOCSY-HSQC and NOESY-HSQC spectra. The use of homonuclear experiments should help to show the effects of these paramagnetic ions without the filter of the heteronucleus. Despite some difficulties in identifying the resonances because of spectral crowding, the diagonal peaks of residues 20, 21, 22, 25, 27–32, 44, 47, 59–61, 75, 78, 90, 103, 105 and 106 seemed to disappear in both experiments at a 0.5 : 1 Eu^{3+}/protein ratio. This was confirmed by HSQC spectra, in which the main effect of the addition of one equivalent of Eu^{3+} to CyaY was severe broadening of resonances 20–31. The resonances of residues 14, 17–19, 32, 33, 34, 42–44 and 106 were shifted. Unspecific broadening became very severe at higher concentrations of lanthanide ion.

When Yb^{3+} was used, we expected large pseudocontact shifts around the binding site [30]. However, adding Yb^{3+} to CyaY did not cause any shift. The diagonal peaks of residues 18–25, 27–34, 40, 44, 65, 66, 101, 103 and 106 disappeared at a 1 : 1 ion/protein ratio in both the TOCSY-HSQC and the NOESY-HSQC spectra. Similar results were obtained with HSQC spectra. At higher Yb^{3+} concentrations, all peaks suffered from severe line broadening.

Titration of CyaY with lanthanides – titration of CyaY with gadolinium

Gd^{3+} has an f^7 configuration in which all f orbitals are half-occupied. Owing to the spherical distribution of the electrons around its nucleus, Gd^{3+} does not cause paramagnetic shifts, but has a powerful effect on the relaxation rates of spatially adjacent atoms. This property makes it, for instance, an excellent relaxation agent in magnetic resonance imaging studies [32]. Titration with this ion was therefore carried out at very low ion/protein ratios. The first point was recorded at a 0.05 : 1 ion/protein ratio, and a small broadening effect was observed on resonances 22, 23 and 33. At a ratio of 0.1 : 1, however, peaks 19, 20–25, 27–29, 31–34, 42–46 noticeably weakened. This effect was even stronger at a 1 : 1 ratio, thus preventing further analysis of the effects (Fig. 2A).

Titration of CyaY with lanthanides – titration of CyaY with lutetium

To investigate the effect of a diamagnetic cation different from Ca^{2+}, we used the lanthanide Lu^{3+}, which has a full f orbital shell with an f^{14} electronic configuration. Lu^{3+} also has an ionic radius very close to that of Yb^{3+}. Surprisingly, we observed disappearance of the resonances of residues 23 and 27 at a 0.5 : 1 Lu^{3+}/CyaY ratio. The resonances of residues 18, 19, 22, 24, 25, 28, 29, 44 and 105 shifted gradually, and were bleached up to disappearance as the titration progressed (up to a 3 : 1 ratio) (Fig. 2B). The resonances of residues 14, 17, 19, 20, 31, 34 and 43 shifted, and those of residues 32, 42, 13 and 24 were affected, but, due to severe overlap, it was impossible to discriminate precisely one from the other. Disappearance of some resonances without the obvious appearance of new signals suggests the presence of an intermediate rate-exchanging equilibrium between the resonances of the metal-bound and the free protein.

Studies in the crystalline state

To obtain a direct structural description of the binding sites, we attempted to obtain CyaY–metal complexes both by direct crystallization and by soaking experiments. The main targets were Fe(II) and Fe(III), but several of the ions used in the solution studies were also tested. Interestingly, no crystals of complexes of CyaY with iron cations could be obtained, despite the several different environmental conditions explored (pH, iron/protein ratios, precipitant agents, soaking time, and ligand concentration). All the crystals from cocrystallization experiments were isomorphous to those of the wild-type, and no sign of deterioration of the diffracting power was observed in the soaking experiments. The presence of metal ions was checked in all trials by anomalous (F_{ano}) and isomorphous (ΔF_{iso}) Fourier maps [33], but none of these methods showed any significant peak, thus indicating that iron cannot easily be trapped in CyaY crystals.

On the other hand, difference maps provided clear evidence of the presence of bound metals when Eu^{3+} or Co^{2+} were used in soaking and cocrystallization experiments, respectively. The statistics of the refined

Table 1. Crystallographic statistics for the structures of CyaY and its Co^{2+} and Eu^{3+} complexes.

	Apo-CyaY in-house	CyaY–Co(II) Elettra	CyaY–Eu(III) Elettra
Diffraction data			
Cell dimensions (Å)[a,b]	43.99, 98.72	43.91, 98.60	43.74, 98.52
Space group	P322(1)	P322(1)	P322(1)
Resolution limits (Å)	20.0–1.87 (1.91–1.87)[a]	30.0–1.75 (1.78–1.75)	30.0–1.42 (1.44–1.42)
No. of observations	65 259	59 856	114 772
No. of unique reflections	8790	11 626	20 848
Completeness (%)	90.8 (93.1)	99.2 (99.6)	97.2 (99.9)
$<I>/<\sigma(I)>$	20.9 (6.4)	29.7 (6.9)	15.9 (3.1)
Multiplicity	7.4	5.2	5.0
R_{merge} (%)[c]	6.8 (17.4)	5.7 (21.2)	8.6 (41.9)
Refined model			
R_{fac}, R_{free} (%)[b]	20.7, 23.6	18.7, 23.0	20.5, 23.2
No. of protein atoms	860	860	860
No. of water molecules	95	75	165
Number of metal ions	–	2	5
Bond lengths (Å)	0.009	0.012	0.010
Bond angles (°)	0.58	1.3	1.3
Protein	13.9	30.0	22.0
Metal ions	–	25.8	27.7
Occupancy of sites M1, M2, M3, M4 and M5	–	0.7, 0.6, 0, 0, 0	0.4, 0.9, 0.9, 0.5, 0.5
Ramachandran plot (%)	93.6 (most favored); 6.4 (additionally allowed)	95.7 (most favored); 4.3 (additionally allowed)	95.7 (most favored); 3.2 (additionally allowed) 1.1 (generously allowed)

[a] Highest-resolution shell given in parentheses. [b] R_{fact} $\Sigma|F_{obs} - F_{calc}|/\Sigma F_{obs}$, where F_{obs} and F_{calc} are the observed and calculated structure factor amplitudes, respectively. R_{free} is the same as R_{fact}, but calculated on 10% of the data excluded from refinement. [c] R_{merge} $\Sigma\, |I_i - \langle I\rangle|/\Sigma I_i$, where I_i is an individual intensity measurement and $\langle I\rangle$ is the average intensity for this reflection.

structures of these derivatives are given in Table 1. The resulting density maps (F_o–F_c, $2F_o$–F_c and OMIT) are generally well defined, with the exception of region 73–77, which is ordered only in the Eu^{3+} complex.

For the Co^{2+} derivative, both the ΔF_{ano} and ΔF_{iso} maps contain two strong peaks (M1 and M2 in Fig. 3A). In M1, the metal ion is octahedrally coordinated to the carboxylate of Asp3 (2.1 Å), to the Nε2 group of His58 (with a bond length of 2.2 Å), and to four water molecules at distances of 2.1, 2.0, 2.1 and 2.0 Å, respectively, with all the coordination valence angles being close to 90° (Fig. 4A). In M2, the cation is bound to the carboxylate oxygen of Glu33 (with a bond length of 2.1 Å) and to four solvent molecules at distances of 2.3, 2.1, 1.8 and 2.3 Å, respectively, having a distorted octahedral geometry with the sixth ligand being undefined (Fig. 4B). Two of the bound water molecules are hydrogen bonded to the carboxylate of Gln97 of a symmetry-related molecule. The protein side chains involved in the coordination sphere display only minor shifts with respect to their positions in the native structure.

In the Eu^{3+} derivative, the difference maps contain five strong peaks (Fig. 3B,C). Two of them are very similar to the M1 and M2 sites of the cobalt complex, except that the Eu^{3+} ion of M1 is displaced by about 2.0 Å with respect to the Co^{2+} position, somewhat closer to the protein surface (Fig. 4C). In this position, the cation is unable to coordinate His58 and establishes a contact with Glu55 (2.8 Å). Of the remaining three sites, M3 is positioned at 6.1 Å from M2, with two intervening water molecules bridging the two ions (Fig. 4D). The coordination sphere of M3 is completed by three other water molecules at distances of 1.6, 2.0 and 1.8 Å, respectively, and by the carboxylate oxygens of Asp31 (2.1 Å) and of Asp29 (2.7 Å). The two aspartate side chains adopt a different conformation with respect to the free protein. M4 and M5 involve residues whose side chains are not well defined in the crystal structure of the apoprotein. In particular, in M4, Eu^{3+} is coordinated by the carboxylate oxygens of Asp23 (2.8 Å and 2.6 Å) and Glu19 (2.7 Å), and two water molecules (1.7 Å and 1.9 Å) (Fig. 4E). In M5, the side chains of Asp76 (1.9 Å) and Asp27 (2.4 Å) of a symmetry-related molecule and four water molecules (1.9 Å, 2.1 Å, 3.1 Å and 3.0 Å) coordinate the cation with an approximate octahedral geometry (Fig. 4F).

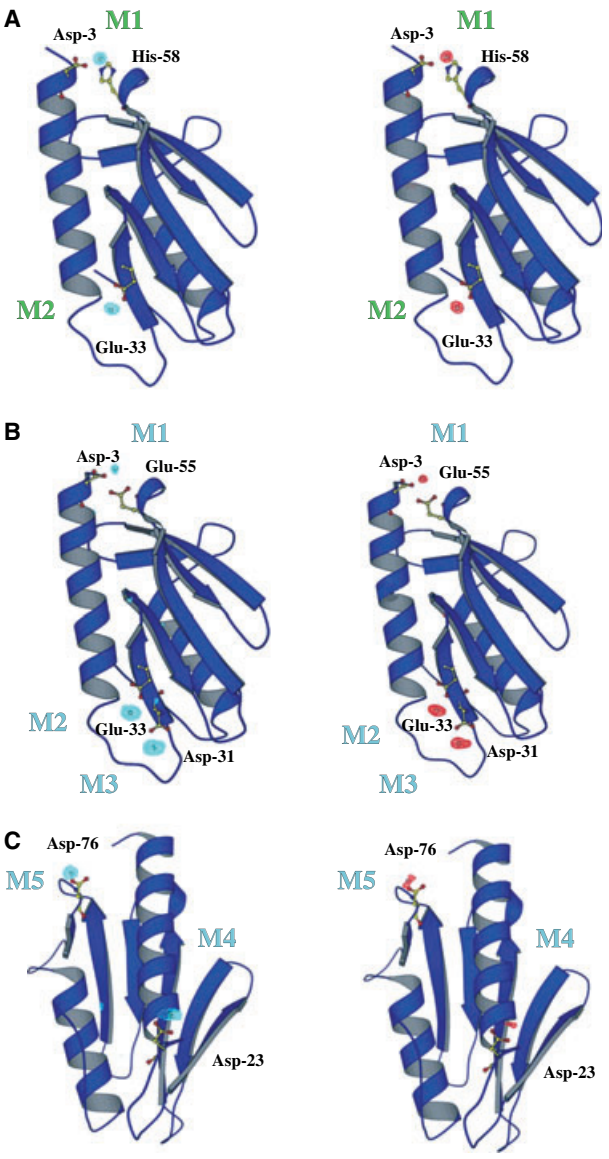

Fig. 3. Ribbon presentation of the three-dimensional structure of the CyaY complexes with Co^{2+} and Eu^{3+}, with corresponding difference Fourier maps for the ions. (A) Observed difference Fourier map for Co^{2+} contoured at 3.0σ above mean level (left) and anomalous difference map for Co^{2+} contoured at 4.0σ above mean level (right). (B, C) Observed difference Fourier maps for Eu^{3+} contoured at 4.0σ above mean level (left) and anomalous difference maps for Eu^{3+} contoured at 6.0σ above mean level (right). The view of (C) is changed to allow appreciation of sites M4 and M5. Protein side chains (ball-and-stick model) that are involved in metal coordination are marked. The figure was generated using BOBSCRIPT [46].

The final models are in both cases very similar to the structures of apo CyaY, as evidenced by the small rmsd values calculated for the main chain atoms, which are not more than 0.2 Å (supplementary Table S1 and Fig. 5A). An interesting feature that is specific to the Eu^{3+} complex regards the perturbation of the hydrophobic core of the molecule, which is induced by ion binding at the M4 site. Rearrangement of the Glu19 and Asp23 side chains influences the main chain of residues 19–22 and produces a rotation of the Leu21 and Trp88 side chains, which is coupled with a small but significant movement of the C-terminal Phe105-Arg106 (Fig. 5B). There is no evidence of a similar structural shift in the complex with Co^{2+}, where only two sites are occupied. These findings indicate a long-range effect of the ion binding to M4, and may explain the perturbation of region 104–106 observed in the NMR studies. On the contrary, no crystallographic indication of an involvement of region 42–44 in metal binding was found.

Discussion

We have studied the interaction of CyaY with different paramagnetic and diamagnetic ions by complementary high-resolution techniques, such as X-ray and NMR techniques. We first probed the interactions in solution, using both diamagnetic and paramagnetic cations. This study is interesting, beyond its significance for understanding the properties of the frataxin family, because of the unusual properties observed.

Ca^{2+} induces only small and well-localized chemical shift perturbations of the CyaY spectrum, mainly at residues 22, 23 and 27–31. These are the same residues that are affected by iron, in agreement with the observation that large concentrations of Ca^{2+} inhibit iron binding [27,28]. Fe(II) and Fe(III) affect the amide resonances in different ways. Fe^{2+} induces both a hyperfine shift (presumably of dipolar origin) and a relaxation enhancement of the signals, whereas Fe^{3+} does not cause chemical shift variations but has exclusively a relaxation effect, indicating that this ion is in a high-spin configuration, with an isotropic distribution of the electrons in its outer shell [30].

When lanthanides were used, one equivalent of Gd^{3+} or Eu^{3+} was sufficient, as expected, to cause large variations in the spectrum, but the effect observed with Yb^{3+} is surprising: although the presence of Yb^{3+} should induce large pseudocontact shifts, no chemical shift variations, which were observed in the presence of Eu^{3+}, were detected. The effect of Lu^{3+} is also peculiar. Being diamagnetic, the ion should not cause paramagnetic shifts or influence the transversal relaxation. Conversely, two equivalents of the ion cause the shift and disappearance of several signals, without the concomitant appearance of any new resonance. This anomalous behavior is likely to

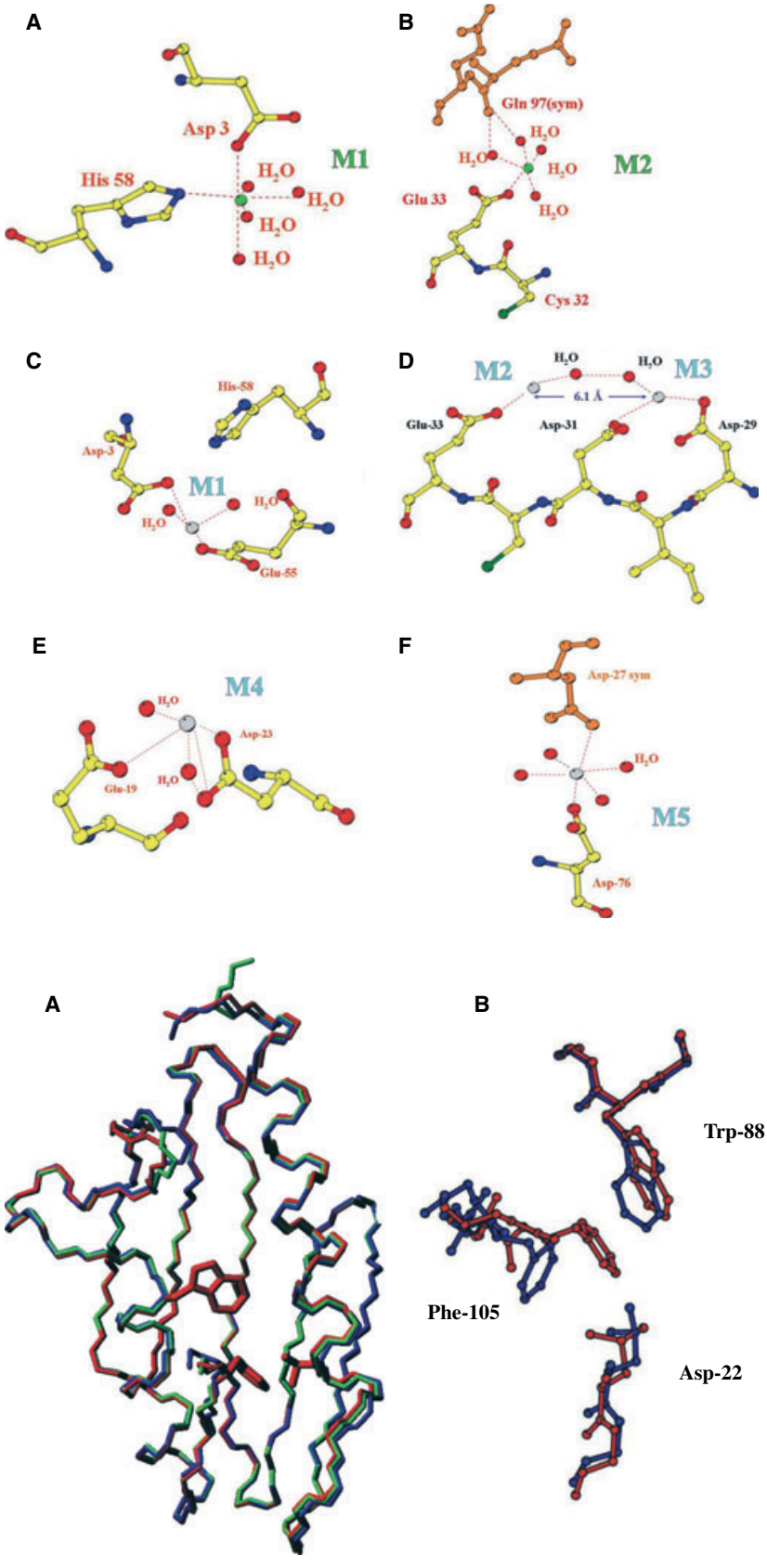

Fig. 4. Metal geometry of the cobalt (green) and europium (pale blue) ions in the corresponding sites. The metal–ligand interactions are marked with dotted lines. The figure was generated using BOBSCRIPT [46].

Fig. 5. Effect of cation binding on the overall CyaY fold. (A) Superposition of Co^{2+} and Eu^{3+} complexes on the apo-CyaY structure (1ew4). The general fold is strongly conserved, with only minor local rearrangements. (B) Details of the superimposition of the hydrophobic core of CyaY (blue) and CyaY–Eu complex (red). The side chains of the CyaY C-terminus rearrange as a long-range effect of binding. The figure was generated using MOLMOL [45] and BOBSCRIPT [46].

be due to the presence of an exchange mechanism between the metal-bound and the free species, due to the low affinities of the complexes involved. The residues that undergo resonance shifts must be involved in a fast equilibrium between different conformations, whereas the peaks that disappear might participate in an intermediate exchange process.

Attempts were made to obtain a more direct description of the ion-binding geometry of CyaY complexes by X-ray crystallography. Curiously, despite exhaustive experimental efforts, crystals of iron derivatives could not be obtained, even though affinity constants in the micromolar range ought to be sufficient to allow crystallization of iron complexes of CyaY. It seems likely that, because it is capable of binding a variety of ions with high charge density, CyaY cannot easily crystallize as a single species, as the multiplicity of binding sites observed by NMR measurements would inevitably lead to a large entropic contribution and a polymorphism that would oppose the tendency of a given well-defined complex to crystallize. Accordingly, the crystal structure obtained by soaking experiments shows a multiplicity of binding sites, some of which should have affinities for ions even lower than those measured spectroscopically [3,26] for iron, as judged from their coordinations, which require several water molecules.

Despite the noncomplete agreement between the sites indicated by the solution studies and those described in the crystal, our structures confirm involvement of the negatively charged residues in α1 and β1 in cation binding, and provide valuable information about the geometries required for such weak complexes: all the sites observed involve exposed residues, as opposed to the majority of the currently known metal–protein complexes, in which the metal is hosted in confined grooves or cavities. In our complexes, either water molecules or a symmetry-related molecule or both are necessary for metal binding. The latter mechanism is likely to be relevant only at the level of aggregate formation (i.e. aerobic conditions, low ionic strength and iron excess), as we know that frataxins are also able to bind iron in their monomeric states [25,27]. Another interesting observation is that, in agreement with the NMR results, all coordination geometries except for that of the M1 site of Co^{2+} involve the side chains of Asp and Glu residues. This feature is again highly unusual for iron chelation, although consistent with the modest affinity constants measured for Fe^{2+} binding [3,26]. The only site that contains a His (M1 for Co^{2+}) has an occupancy that is comparable to if not lower than those of the others (Table 1). This is also in contrast with the sites identified by Karlberg *et al.* in the trimeric structure of Tyr73Ala Yfh1 [34], none of which, apart from M5 of the Eu^{3+} structure, has any apparent resemblance to the ones identified in our structures. The iron-loaded trimer of Tyr73Ala Yfh1 contains one iron ion located in the channel formed by trimerization. Although the authors hypothesize that some of the residues lining the cleft may be involved in the delivery of the ion, the only acidic residue close by is Asp143, which corresponds to Asp76 in CyaY (see Eu^{3+} M5). This suggests that the structure of the trimer might have been induced by mutation, and does not necessarily resemble an *in vivo* situation.

The picture that results from our study is that CyaY and, given the high homology within the family, frataxins in general constitute a new type of metal-binding protein, the properties of which are very different from those of canonical families. They bind ions with low affinity and even lower specificity, and contain multiple binding sites. The binding mechanism is exclusively electrostatically driven, in agreement with the conserved acidic pI of frataxins and with the only partial conservation of the acidic residues around the ridge defined as α1 and β1, which are those involved in binding. The precise positions of negatively charged residues could be not so important, provided that equivalent areas in different orthologs retained a similar overall charge density.

Such a model of a 'delocalized' binding site within a cooperative mechanism would also be consistent with a cooperative mechanism in which the copresence of several sites is essential for functioning. In full agreement with this view is the observation that single mutations of the acidic residues involved in iron binding can be tolerated with regard to the preservation of frataxin function, whereas multiple mutations of key acidic residues are catastrophic for *in vivo* activity: recently, analyzing iron-binding properties within the complex formed by Nfs1, Isu1 and yfh1 *in vivo*, we demonstrated that the acidic ridge that contains α1 and β1 is involved in Fe–S cluster assembly [35]. In addition, we showed that when acidic residues on both sides of the negatively charged patch (in the D86K/E89K, D101K/E103K and D86A/E89A/ D101A/E103A Yfh1 mutations, which affect residues equivalent to E19, D22, D31 and D33 in CyaY) are mutated, there is a marked loss of function. We concluded that an appropriate acidic environment is required for the function of frataxin in Fe–S cluster assembly, and proposed that these residues have a crucial role as the cradle for Fe–S cluster formation. This evidence, together with that reported in the present article, suggests a new perspective on the functions of frataxin *in vivo*, and could help in their further characterisation.

Experimental procedures

Protein production

The protein was produced as previously described [24]. $Fe(NH_4)_2(SO_4)_2$, $FeCl_3$, $CaCl_2$, $Mg(SO_4).7H_2O$, $CoSO_4.7H_2O$, $MnSO_4.4H_2O$, $Zn(SO_4)_2.7H_2O$ and $LuCl_3$ were purchased from Sigma-Aldrich (Gillingham, UK). $EuCl_3$, $YbCl_3$ and $GdCl_3$ were purchased from Strem Chemicals (Newburyport, MA, USA).

NMR spectroscopy

The NMR spectra were typically performed on 0.5–0.8 mM samples uniformly labeled with ^{15}N, in 90% H_2O/10% D_2O solutions containing either 20 mM Tris/HCl or 10 mM Hepes, and 50 mM NaCl (pH 7–7.5). All NMR experiments were performed at 25 °C on Varian Unity, Unityplus and Inova spectrometers (Varian, Palo Alto, CA, USA) operating at 500, 600 and 800 MHz proton frequencies and equipped with 5 mm triple-resonance probes. The spectra were processed and analysed using NMRPIPE [36] and XEASY software [37].

The effects of the different cations were assessed by performing HSQC experiments typically with 80 increments in the indirect dimension. When indicated, 3D[^1H,^{15}N] NOESY-HSQC and TOCSY-HSQC spectra (with 100 ms and 70 ms mixing times, respectively) were also recorded. Iron titrations were performed under both aerobic [Fe(II) or Fe(III)] and anaerobic [Fe(II)] conditions. When anaerobic conditions were explored, the samples were prepared in a glove box filled with argon (Belle Technology, Portesham, UK). Each experiment was repeated at least three times to ascertain reproducibility.

Crystallography studies

CyaY was crystallized at 20 °C by vapor diffusion under conditions very similar to those previously reported [26]. Sitting drops were buffered with 0.1 M sodium acetate (pH 4.5–5.0), containing 200 mM $CaCl_2$, 30% w/v poly(ethylene glycol) 4000, and 2 mM β-mercaptoethanol. The protein concentration was in the range 15–20 $mg{\cdot}mL^{-1}$. Large crystals grew after few days from an amorphous precipitate, which formed shortly after the experiment had been set up. New crystallization conditions were also found: crystals were grown by vapor diffusion using equal volumes of the protein sample (20 $mg{\cdot}mL^{-1}$) and a solution containing 2.0 M ammonium sulfate, 0.1 M sodium acetate (pH 4.5–5.0), and 2–4% v/v sucrose.

Both cocrystallization and soaking procedures were used in attempts to obtain crystals of the iron complex. Cocrystallization experiments were performed using either poly(ethylene glycol) 4K or ammonium sulfate as precipitant agents, and iron in either oxidation state (CyaY/Fe molar ratios: 1 : 2, 1 : 4, 1 : 6). At the same time, the diffusion of iron [Fe(II) and Fe(III)] in protein crystals grown from poly(ethylene glycol) 4K or from ammonium sulfate was tried. The soaking experiments were performed at crystallization pH (4.5–5.0) and physiologic pH (7.0–7.5) after slow equilibration of the crystals in the stabilizing solution. Different soaking times were tried (1 h to 1 week). The iron concentration was estimated by a photometric assay with 1,10-phenanthroline. All the trials with Fe(II) were performed in a glove-box (MBRAUN Glovebox Technology, Garching, Germany). The cocrystallization and soaking trials were performed in the absence of $CaCl_2$.

CyaY/Co^{2+} crystals were grown by cocrystallization from poly(ethylene glycol) 4K with the addition of $CoCl_2$ instead of $CaCl_2$. CyaY/Eu^{3+} crystals were prepared by soaking for 45 min protein crystals from poly(ethylene glycol) 4K in the appropriate mother liquor saturated with $EuCl_3$.

All X-ray data were collected on cryocooled crystals using either a DIP-2030 Enraf-Nonius (Delft, the Netherlands) detector in-house X-ray source (monochromated CuKa radiation) or an MAR Research CCD detector (Norderstedt, Germany) at the Elettra synchrotron source (Trieste, Italy). A native dataset was collected at 1.87 Å resolution on a crystal grown from poly(ethylene glycol) 4K. For both complexes, an initial dataset was collected in house, and a second one at higher resolution was collected at the Elettra synchrotron in Trieste. The datasets were indexed and integrated with DENZO, and scaled by SCALEPACK [38]. Statistics of the data collected on the free enzyme and on the two complexes at higher resolution are summarized in Table 1. Ten per cent of the dataset was used to monitor R_{free}.

The native protein structure was refined using the CNS package [39] and starting from the 1ew4 dataset [23]. This model was used for the structure refinement of the metal complexes by the SHELXL program [40]. Anisotropic temperature factors were used only for the metal ions. The presence of metal ions was ascertained by means of anomalous difference maps (ΔF_{ano}) [32] calculated with the Collaborative Computational Project Number 4 (CCPN4) suite [41], using the phases of the refined native protein model. The difference Fourier maps (ΔF_{iso}) were also inspected with coefficients $(F_2–F_1)\ \exp(-i\varphi_{calc1})$, where F_2 and F_1 are the observed structure factors of the complex and protein, respectively, and φ_{calc1} is the calculated phase of the protein model.

The program O software [42] was used for map inspection and model building. Only water molecules with well-defined density and a reasonable hydrogen bond geometry were included in the refinement. The correctness of the model was checked using the PROCHECK [43] and WHATCHECK [44] programs. The coordinates of the higher-resolution complex models have been deposited in the Protein Data Bank (2EFF and 2P1X for the complexes with cobalt and europium, respectively).

Acknowledgements

The authors are indebted to John McCormick for production of the protein and Lelio Mazzarella for continuous encouragement and support. A. Pastore was funded by a FARA/MDA grant. F. Sica and P. Temussi were funded by MIUR (FIRB 2003, Progetto RBNE03B8KK).

References

1 Campuzano V, Montermini L, Molto MD, Pianese L, Cossée M, Cavalcanti F, Monros E, Rodius F, Duclos F, Monticelli A *et al.* (1996) Friedreich's ataxia: autosomal recessive disease caused by an intronic GAA triplet repeat expansion. *Science* **271**, 1423–1427.

2 Cossee M, Puccio H, Gansmuller A, Koutnikova H, Dierich A, LeMeur M, Fischbeck K, Dolle P & Koenig M (2000) Inactivation of the Friedreich ataxia mouse gene leads to early embryonic lethality without iron accumulation. *Hum Mol Genet* **9**, 1219–1226.

3 Yoon T & Cowan JA (2003) Iron–sulfur cluster biosynthesis. Characterization of frataxin as an iron donor for assembly of [2Fe–2S] clusters in ISU-type proteins. *J Am Chem Soc* **125**, 6078–6084.

4 Yoon T & Cowan JA (2004) Frataxin-mediated iron delivery to ferrochelatase in the final step of heme biosynthesis. *J Biol Chem* **279**, 25943–25946.

5 Bulteau AL, O'Neill HA, Kennedy MC, Ikeda-Saito M, Isaya G & Szweda LI (2004) Frataxin acts as an iron chaperone protein to modulate mitochondrial aconitase activity. *Science* **305**, 242–245.

6 Gerber J, Muhlenhoff U & Lill R (2003) An interaction between frataxin and Isu1/Nfs1 that is crucial for Fe/S cluster synthesis on Isu1. *EMBO Reports* **4**, 906–911.

7 Park S, Gakh O, O'Neill HA, Mangravita A, Nichol H, Ferreira GC & Isaya G (2003) Yeast frataxin sequentially chaperones and stores iron by coupling protein assembly with iron oxidation. *J Biol Chem* **278**, 31340–31351.

8 Park S, Gakh O, Mooney SM & Isaya G (2002) The ferroxidase activity of yeast frataxin. *J Biol Chem* **277**, 38589–38595.

9 Cavadini P, O'Neill HA, Benada O & Isaya G (2002) Assembly and iron-binding properties of human frataxin, the protein deficient in Friedreich's ataxia. *Hum Mol Genet* **11**, 217–227.

10 Delatycki MB, Williamson R & Forrest SM (2000) Freidreich's ataxia: an overview. *J Med Genet* **37**, 1–8.

11 Huynen MA, Snel B, Bork P & Gibson TJ (2001) The phylogenetic distribution of frataxin indicates a role in iron–sulfur cluster protein assembly. *Hum Mol Genet* **10**, 2463–2468.

12 Muhlenhoff U, Richhardt N, Ristow M, Kispal G & Lill R (2002) The yeast frataxin homolog Yfh1p plays a specific role in the maturation of cellular Fe/S proteins. *Hum Mol Genet* **11**, 2025–2036.

13 Stehling O, Elsasser H-P, Bruckel B, Muhlenhoff U & Lill R (2004) Iron–sulfur protein maturation in human cells: evidence for a function of frataxin. *Hum Mol Genet* **13**, 3007–3015.

14 Wong A, Yang J, Cavadini P, Gellera C, Lonnerdal B, Taroni F & Cortopassi G (1999) The Friedreich's ataxia mutation confers cellular sensitivity to oxidant stress which is rescued by chelators of iron and calcium and inhibitors of apoptosis. *Hum Mol Genet* **8**, 425–430.

15 Ristow M, Pfister MF, Yee AJ, Schubert M, Michael L, Zhang C-Y, Ueki K, Michael MD 2nd, Lowell BB & Kahn CR (2000) Frataxin activates mitochondrial energy conversion and oxidative phosphorylation. *Proc Natl Acad Sci USA* **97**, 12239–12243.

16 Tan G, Napoli E, Taroni F & Cortopassi G (2003) Decreased expression of genes involved in sulfur amino acid metabolism in frataxin-deficient cells. *Hum Mol Genet* **12**, 1699–1711.

17 Lesuisse E, Santos R, Matzanke BF, Knight SAB, Camadro J-M & Dancis A (2003) Iron use for heme synthesis is under control of the yeast frataxin homologue (Yfh1). *Hum Mol Genet* **12**, 879–889.

18 Radisky DC, Babcock MC & Kaplan J (1999) The yeast frataxin homologue mediates mitochondrial iron efflux: evidence for a mitochondrial iron cycle. *J Biol Chem* **274**, 4497–4499.

19 Foury F & Talibi D (2001) Mitochondrial control of iron homeostasis. A genome wide analysis of gene expression in a yeast frataxin-deficient strain. *J Biol Chem* **276**, 7762–7768.

20 Que L Jr & Ho RY (1996) Dioxygen activation by enzymes with mononuclear non-heme iron active sites. *Chem Rev* **96**, 2607–2624.

21 Musco G, Stier G, Kolmerer B, Adinolfi S, Martin S, Frenkiel T, Gibson T & Pastore A (2000) Towards a structural understanding of Friedreich's ataxia: the olution structure of frataxin. *Structure* **8**, 695–707.

22 Dhe-Paganon S, Shigeta R, Chi Y-I, Ristow M & Shoelson SE (2000) Crystal structure of human frataxin. *J Biol Chem* **275**, 30753–30756.

23 Cho SJ, Lee MG, Yang JY, Song HK & Suh SW (2000) Crystal structure of Escherichia coli CyaY reveals a previously unidentified fold for the evolutionary conserved frataxin family. *Proc Natl Acad Sci USA* **97**, 8932–8937.

24 Nair M, Adinolfi S, Pastore C, Kelly G, Temussi P & Pastore A (2004) Solution structure of the bacterial frataxin ortholog, CyaY: mapping the iron binding sites. *Structure (Camb)* **12**, 2037–2048.

25 He Y, Alam SL, Proteasa SV, Zhang Y, Lesuisse E, Dancis A & Stemmler TL (2004) Yeast frataxin solution

structure, iron binding and ferrochelatase interaction. *Biochemistry* **43**, 16254–16262.
26 Bou-Abdallah F, Adinolfi S, Pastore A, Laue TM & Chasteen DN (2004) Iron binding and oxidation kinetics in frataxin CyaY of Escherichia coli. *J Mol Biol* **341**, 605–615.
27 Adinolfi S, Trifuoggi M, Politou AS, Martin S & Pastore A (2002) A structural approach to understanding the iron-binding properties of phylogenetically different frataxins. *Hum Mol Genet* **11**, 1865–1877.
28 Adinolfi S, Nair M, Politou A, Bayer E, Martin S, Temussi P & Pastore A (2004) The factors governing the thermal stability of frataxin orthologues: how to increase a protein's stability. *Biochemistry* **43**, 6511–6518.
29 Butchard CG, Dwek RA, Ferguson SJ, Kent PW, Williams RJP & Xavier AV (1972) Mapping of the binding site of N-fluoroacetyl-d-glucosamine and analogues in hen egg lysozyme by 1H and 19F-NMR techniques with Gd(III) and Mn(II) as paramagnetic probes. *FEBS Lett* **25**, 91–93.
30 Bertini I & Luchinat C (1996) NMR of paramagnetic substances. *Coord Chem Rev* **150**, 1.
31 Saito T, Wormald MR & Williams RJ (1991) Some structural features of the iron-uptake regulation protein. *Eur J Biochem* **197**, 29–38.
32 Evans CH (1990) *Biochemistry of the Lanthanides*. Plenum Press, New York, NY.
33 Carter CW Jr & Sweet RM (1997) Macromolecular crystallography. Part A. *Methods Enzymol* **276**, 530–538.
34 Karlberg T, Schagerlof U, Gakh O, Park S, Ryde U, Lindahl M, Leath K, Garman E, Isaya G & Al-Karadaghi S (2006) The structures of frataxin oligomers reveal the mechanism for the delivery and detoxification of iron. *Structure* **14**, 1535–1546.
35 Foury F, Pastore A & Trincal M (2007) Acidic residues of yeast frataxin have an essential role in Fe–S cluster assembly. *EMBO Report* **8**, 194–199.
36 Delaglio F, Grzesiek S, Vuister G, Zhu G, Pfeifer J & Bax A (1995) NMRPipe: a multidimensional spectral processing system based on UNIX pipes. *J Biomol NMR* **6**, 277–293.
37 Bartels Ch, Xia T-H, Billeter M, Güntert P & Wüthrich K (1995) The program XEASY for computer-supported NMR spectral analysis of biological macromolecules. *J Biomol NMR* **5**, 1–10.
38 Otwinowski Z & Minor W (1997) Processing of X-ray diffraction data collected in oscillation mode. *Methods Enzymol* **276**, 307–326.
39 Brünger AT, Adams PD, Clore GM, DeLano WL, Gros P, Grosse-Kunstleve RW, Jiang J-S, Kuszewki JJ, Nilges M, Pannu NS *et al.* (1998) Crystallography and NMR system: a new software suite for macromolecular structure determination. *Acta Crystallogr* **54D**, 905–921.
40 Schneider TR & Sheldrick GM (2002) Substructure solution with SHELXD. *Acta Crystallogr D Biol Crystallogr* **58**, 1772–1779.
41 Collaborative Computational Project Number 4 (1994) The CCP4 suite: programs for protein crystallography. *Acta Crystallogr D Biol Crystallogr* **50**, 760–763.
42 Jones TA, Zou JY, Cowan SW & Kjeldgaard M (1991) Improved methods for building protein models in electron density maps and the location of errors in these models. *Acta Crystallogr* **A47**, 110–119.
43 Laskowski RA, MacArthur MW, Moss DS & Thornton JM (1993) PROCHECK: a program to check the stereochemical quality of protein structure. *J Appl Crystallogr* **26**, 283–291.
44 Hooft RW, Vriend GS & Abola EE (1996) Errors in protein structures. *Nature* **381**, 272.
45 Koradi R, Billeter M & Wüthrich K (1996) MOLMOL: a program for display and analysis of macromolecular structure. *J Mol Graph* **14**, 51–55.
46 Esnouf RM (1999) Further additions to Molscript, Version 1.4, including reading and contouring of electron-density maps. *Acta Crystallogr* **D55**, 938–940.

Supplementary material

The following supplementary material is available online:

Fig. S1. CyaY titration with Zn^{2+}.

Table S1. RMSD after backbone superimposition.

This material is available as part of the online article from http://www.blackwell-synergy.com

Please note: Blackwell Publishing is not responsible for the content or functionality of any supplementary materials supplied by the authors. Any queries (other than missing material) should be directed to the corresponding author for the article.